# Adjoint-based Anisotropic Mesh Adaptation for a Stabilized Finite-Element Flow Solver

Aravind Balan,* Michael A. Park,† and W. Kyle Anderson‡
*NASA Langley Research Center, Hampton, VA 23681, USA*

**An adjoint solver is implemented in the FUN3D stabilized finite-element flow solver. The adjoint solution is used to generate anisotropic, adapted meshes to control error in scalar output functionals, such as lift or drag coefficient. The inviscid and turbulent adjoints are verified with a finite-difference derivative approximation and can be used in design optimization in addition to mesh adaptation. The adjoint capability represents an extension of previous research using the FUN3D stabilized finite-element capability with metric-based mesh adaptation and interpolation-based error estimates to generate highly anisotropic adapted meshes for turbulent flows. In the present work, a metric-based approach is again utilized, where the adjoint and the primal solutions both contribute to the generation of a metric tensor field that is subsequently used to produce the required anisotropic mesh for each adaptation cycle. Adaptive results are then shown for an inviscid supersonic flow over a diamond airfoil, inviscid transonic flow over the ONERA M6 wing, and viscous laminar flow over the NACA 0012 airfoil, all using drag force as the output functional. Adjoint-based adaptation is compared with a multiscale solution-based approach that controls the $L_p$ norm of Mach number interpolation error to demonstrate the effectiveness and efficiency of the adjoint-based adaptive mesh technology.**

## I. Introduction

Advancements in computational power, and increased research on numerical algorithms, have enabled widespread application of Computational Fluid Dynamics (CFD) simulations for aerospace design. Despite the fact that significant capabilities now exists, performing high-fidelity CFD simulations for complex aerospace configurations remains computationally expensive. The CFD Vision 2030 Study: A Path to Revolutionary Computational Aerosciences [1] proposes a research strategy for developing visionary CFD capability by the year 2030. The CFD Vision 2030 study specifically identifies mesh generation and adaptive-mesh technology to be significant bottlenecks in the current CFD work flow. To this end, the present work aims to incorporate adjoint-based anisotropic mesh adaptation capabilities into stabilized finite-element (SFE) capability [2] of Fully Unstructured Navier-Stokes 3D (FUN3D) [3], which will subsequently be referred to in the remainder of the text as FUN3D-SFE.

Mesh adaptation is a means for decreasing the cost of turbulent flow simulations by providing an effective tool for systematically reducing discretization errors without requiring continual manual intervention on a series of globally refined meshes. For fluid dynamics, especially in aerodynamic applications, highly anisotropic flow features, such as boundary layers and shock waves, mandate that the mesh also exhibit strong directionality for sufficient resolution. In the context of aerodynamic flow simulations using high-order discontinuous Galerkin methods, Leicht and Hartmann [4] have demonstrated the potential of adjoint-based error estimators and anisotropic mesh refinement. In their method, the mesh elements are split in specific directions, given by anisotropic indicators, to achieve the required directionality along flow features. The concept of continuous mesh and mesh-metric duality [5, 6] provides a well-posed alternative to directly specifying discrete splits, where metric tensor fields encode information about the mesh elements that includes their size, anisotropy and orientation to generate anisotropic simplex mesh elements. In the adaptation procedure, metric tensors for the desired mesh are evaluated using the solution, and optionally adjoint, from the current simulation, and these metric tensors are then passed to a metric-conforming mesh generator to generate the required anisotropic mesh.

The main advantage of using metric-based mesh adaptation is the flexibility it provides in manipulating the size and the shape of mesh elements. Loseille et al. [7] demonstrated the potential of metric-based anisotropic mesh adaptation using several three-dimensional test cases. Fidkowski and Darmofal [8] provide an excellent summary of various techniques for doing anisotropic mesh adaptation based on output error estimators of CFD simulations.

*NASA Postdoctoral Fellow, AIAA Member.
†Research Scientist, Computational AeroSciences Branch, AIAA Associate Fellow.
‡Senior Research Scientist, Computational AeroSciences Branch, AIAA Associate Fellow.

Alauzet and Loseille [9] review the progress made in anisotropic mesh adaptation for CFD during the last decade. In a more recent paper, Park et al. [10] review the status of unstructured grid adaptation, identify the impact of robust automated unstructured grid technologies, and recommend the adoption of newly developed and matured unstructured grid adaptation technologies with an intent of contributing to the CFD 2030 Vision Study capabilities mentioned in [1]. Park et al. [11] examined the anisotropic mesh adaptation by decomposing the adaptation cycle into individual steps consisting of flow and adjoint solution, error estimation, metric construction and mesh generation (see Fig. 1). Multiple implementations of each of these steps were compared to each other. This comparison was followed by the verification of various anisotropic mesh adaptation tools using several test cases including RANS solutions on a hemisphere cylinder [12], laminar solutions on a delta wing, and RANS solutions on the ONERA M6 wing [13]. Independently implemented mesh adaptation procedures showed consistent convergence to fine-grid forces and moments for each of these test cases, and adjoint-based metrics that control the estimates of output quantities (drag or lift) converged faster to fine-grid forces than the multiscale metric that controlled the interpolation error of Mach number.

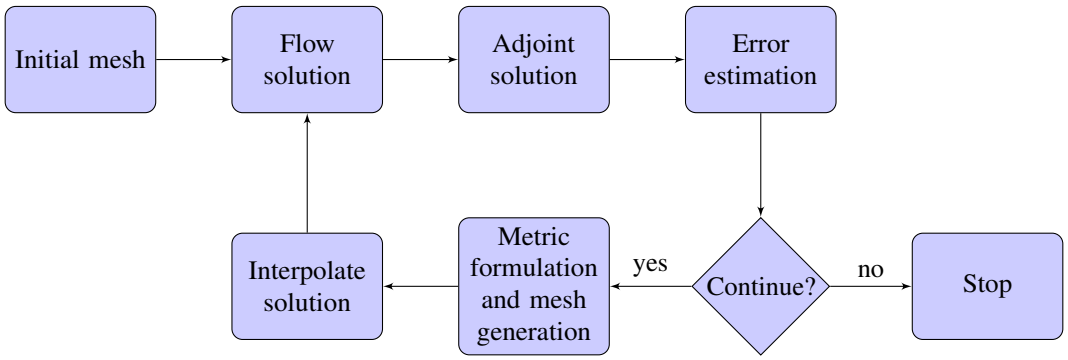


**Fig. 1 Adjoint-based anisotropic grid adaptation process.**

The adjoint-based implementation for mesh adaptation in the present work closely follows the approach of Loseille et al. [7] in which the metric field is formulated using the information from the adjoint variables and from the flux functions for 3D steady Euler equations. Comparisons are made with adaptations based on a multiscale metric approach that controls interpolation error of a scalar field, typically Mach number [14].

The remainder of this paper is organized as follows. The general adaptation methodology is described in Section II, which includes a brief description of the flow and adjoint solvers, metric construction and adaptive mesh generation. Verification of the adjoint formulation, using finite differences, is presented for both inviscid and turbulent flows. Adaptive results are then presented for an inviscid supersonic flow over a diamond airfoil, inviscid transonic flow over the ONERA M6 wing and viscous laminar flow over the NACA0012 airfoil, using drag force as the output functional. Results are also compared with those obtained using a solution-based approach, that controls the $L_p$ norm of Mach number interpolation error, to evaluate the effectiveness and efficiency of the adjoint-based adaptive mesh technology.

## II. Adaptation Method

The components of adjoint-based anisotropic mesh adaptation are shown in Fig. 1. Beginning with an initial mesh, a flow solution is computed using the FUN3D-SFE solver, after which the adjoint solution is computed for a specified output functional. The flow solution and the adjoint solution are then used to estimate error. If the estimated errors are larger than limits specified by the practitioner, a metric tensor field that encodes the information for a desired mesh is generated from the flow and the adjoint solution, and the current mesh is modified to adhere to the metric field. Once the adapted grid is available, the previous flow solution can be interpolated to the new grid to provide an initial condition for the flow solver for the next adaptive cycle. This improved initial condition decreases the execution time and improves the robustness of the flow solution calculation. The process is repeated until an exit criteria is met (e.g., accuracy requirement or resource limit). An overview of the implementations of each of these components is given in the following subsections.

### A. FUN3D-SFE Primal and Adjoint Solver

FUN3D-SFE is based on a stabilized finite-element approach that includes the Streamlined Upwind Petrov-Galerkin (SUPG) scheme [15, 16], Galerkin least squares [17], and variational multiscale methods [18]. In the results shown here, only the SUPG scheme is considered. A linear nodal finite-element basis is used, which is designed to be second-order accurate in space. The current implementation includes the capability for computing on tetrahedra, hexahedra, pyramids, and prisms, although all the results shown in the present paper are for pure tetrahedral grids. The negative SA turbulence model [19] is tightly coupled with the RANS flow equations, yielding a nonlinear algebraic system of equations with six variables at each mesh point, which is solved using a Newton-type approach described in [2].

The discrete adjoint solution, $\lambda_h$, for a particular output functional $I$, is obtained by solving the linear system of equations

$$\left[\frac{\partial R_h}{\partial w_h}\right]^T \lambda_h = \left(\frac{\partial I}{\partial w_h}\right)^T \tag{1}$$

where $w_h$ is the set of solution state variables, and $R_h$ is the discrete residual of the partial differential equations under consideration. Because a Newton-type solver is used for the primal solution, the linearization of the discrete residual is already available and has been verified using operator overloading, hand differentiation, and complex variables. For the adjoint, the Jacobian is transposed to obtain the matrix on the left-hand side of Eq. (1), whereas the right-hand side is obtained using operator overloading. The linear system is solved using the same GMRES algorithm as the flow solver, along with an Incomplete Lower/Upper (ILU) preconditioner that is used for the primal problem.

The implementation of the adjoint has been verified by comparing the adjoint values, obtained by solving Eq. (1), with those obtained using a finite-difference method. Here, the discrete adjoint state represents the sensitivity of the output functional with respect to a perturbation in the discrete residual. To evaluate the terms in the following tables, the solution to the forward problem is first converged to machine precision. The discrete residual at a particular point in the flowfield is then perturbed by a small amount, and new solution variables are obtained by solving the following system of equations for $\Delta w_h$, which is then added to the previous solution to evaluate an updated value of the output function.

$$\left[\frac{\partial R_h}{\partial w_h}\right] \Delta w_h = -R_h \tag{2}$$

The difference in the output functional is then formed, which is used to evaluate the adjoint using finite differences. Tables 1 and 2 show the adjoint values obtained from solving the discrete adjoint equation (Eq. (1)) compared to values obtained using finite differences at a few random positions in the adjoint state vector. Table 1 demonstrates results for the inviscid test case described in Section IV, whereas Table 2 demonstrates results for a turbulent flow. In both cases, a step size of $1.0 \times 10^{-5}$ is used for the finite-difference computations, and the results computed using both methods are seen to be in very good agreement, with the largest difference being less than three significant digits, which corresponds to less than 0.08 percent error.

**Table 1 Adjoint values obtained from adjoint solver and finite difference, inviscid Euler.**

| Sample no. | Adjoint solver | Finite difference |
|---|---|---|
| 1 | -0.3396625 | -0.3394 |
| 2 | 0.0654442 | 0.0654 |
| 3 | -0.1575706 | -0.1576 |
| 4 | -0.3337737 | -0.3337 |
| 5 | 0.4973052 | 0.4975 |
| 6 | -0.1904250 | -0.1904 |

### B. Metric Field Formulation and Mesh Adaptation

The multiscale metric used in the present work was originally developed by Loseille et al. [14]. Adaptated solutions using the multiscale metric are used to compare with solutions obtained using a goal-oriented metric that will be described later in this section. The multiscale metric aims to control the $L^p$-norm of the interpolation error of a solution scalar field. The metric field, $\mathcal{M}_{L^p}$, is constructed from the (reconstructed) Hessian, $H$, of the scalar field that is locally

**Table 2 Adjoint values obtained from adjoint solver and finite difference, turbulent RANS.**

| Sample no. | Adjoint solver | Finite difference |
|---|---|---|
| 1 | -0.2260129 | -0.2260 |
| 2 | 0.9290755 | 0.9297 |
| 3 | 0.2267752 | 0.2268 |
| 4 | -0.4260210 | -0.4261 |
| 5 | 0.1074713 | 0.1074 |
| 6 | 0.2563785 | 0.2566 |

scaled by the Hessian determinant and globally scaled to a specified target to get,

$$\mathcal{M}_{L^p}(\mathbf{x}) = D_{L^p}\,(\det|H(\mathbf{x})|)^{\frac{-1}{2p+3}}\,|H(\mathbf{x})|, \tag{3}$$

where the global scaling $D_{L^p}$,

$$D_{L^p} = \left(\frac{C_t}{\int_\Omega (\det|H(\mathbf{x})|)^{\frac{p}{2p+3}}\,d\mathbf{x}}\right)^{\frac{2}{3}} \tag{4}$$

corrects the complexity of the locally scaled Hessian to produce $\mathcal{M}_{L^p}$ with specified target complexity $C_t$. The complexity $C$ of a continuous metric field $\mathcal{M}$ is defined as the integral

$$C(\mathcal{M}) = \int_\Omega \sqrt{\det(\mathcal{M})}d\mathbf{x}. \tag{5}$$

The complexity can be interpreted as the continuous counterpart of the number of vertices in the discrete mesh. The relationship between the metric complexity $C$ and the number of vertices and elements in the adapted grid is shown theoretically in Ref. [5], and experimentally in Refs. [6, 11]. A grid conforming to $\mathcal{M}_{L^p}$ provides optimal control of the scalar field interpolation error in the $L^p$-norm. A lower $p$-norm targets weaker variations of the scalar field and a larger $p$-norm targets rapid variations of the scalar field [14]. Mesh adaptations using the multiscale metric have been performed for various problems of increasing complexities, that have proven its viability. The various implementations of the multiscale metric have also been verified for turbulent RANS benchmark problems [13]. For the numerical simulations presented in this paper, Mach number is chosen as the scalar field.

For the goal-oriented adaptations for the inviscid flow cases, the approach reported by Loseille et al. [7] is utilized. The approach involves an *a priori* error estimate of output functionals for the Euler equations, and its optimization in the continuous mesh framework using calculus of variations, resulting in an analytical formulation for the metric field. The resulting metric field essentially consists of the sum of Hessians of the Euler fluxes, weighted by the gradient components of the adjoint fields. The complexity of the metric, which directly correlates with the number of mesh nodes, is computed, and the metric is globally scaled to set its complexity to a specified value. The method has been successfully applied to inviscid supersonic flows including a supersonic business jet [9], and a low-boom geometry from the AIAA sonic boom workshop [20], with pressure signatures as the output functional, and demonstrated its efficiency over interpolation error-based multiscale metric adaptations. The mathematical formulation of the metric field $\mathcal{M}_{Go}$, referred as the inviscid goal-oriented metric, is recapitulated here.

$$\mathcal{M}_{Go}(\mathbf{x}) = D_{Go}(\det|M(\mathbf{x})|)^{\frac{-1}{5}}|M(\mathbf{x})| \tag{6}$$

where

$$M(\mathbf{x}) = \sum_{j=1}^{5}\left(\left|\frac{\partial\lambda_j}{\partial x}\right|.|H(F_{j,x}(w))| + \left|\frac{\partial\lambda_j}{\partial y}\right|.|H(F_{j,y}(w))| + \left|\frac{\partial\lambda_j}{\partial z}\right|.|H(F_{j,z}(w))|\right). \tag{7}$$

$\lambda_j$ denotes the $j^{\text{th}}$ component of the adjoint vector $\lambda$, $H$ is the Hessian, and $F_{j,x}, F_{j,y}, F_{j,z}$ are the $x, y$, and $z$ fluxes of

the $j^{th}$ component of the discrete Euler equations. $D_{Go}$ is the global normalization constant given as

$$D_{Go} = \left( \frac{C_t}{\int_\Omega (\det|M(\mathbf{x})|)^{\frac{1}{5}} \, d\mathbf{x}} \right)^{\frac{2}{3}} \tag{8}$$

where $C_t$ is the target complexity. For the viscous case, the inviscid fluxes in the goal-oriented metric (Eq.6) are augmented with the viscous fluxes to perform the adaptation. The convergence of the output quantity is compared with the inviscid goal-oriented metric and the multiscale metric.

For the metrics described above, i.e., multiscale and goal-oriented metrics, the Hessian has to be reconstructed. In the present work, this is done using a k-exact quadratic reconstruction [21] over vertices that are neighbors of neighbors of the vertex having its Hessian reconstructed. The discrete metric field values are computed at the vertices of the current mesh are used as inputs to the metric conforming mesh generator to produce the next mesh. The *refine* open source grid-adaptation mechanics package developed by NASA, is currently used as the metric-conforming mesh generator. *refine* is available via `github.com/NASA/refine` under the Apache License, Version 2.0. It is designed to output a unit grid [5] in a provided metric field. The current version under development uses the combination of edge split and collapse operations proposed by Michal and Krakos [22]. Node relocation is performed to improve adjacent element shapes. A new ideal node location of the node is created for each adjacent element. A convex combination of these ideal node locations is chosen to yield a new node location update that improves the element shape measure in the anisotropic metric [23]. Geometry is accessed through the Electronic Geometry Aircraft Design System (EGADS) [24] application program interface.

## III. Numerical Results - Inviscid Supersonic Flow over a Diamond Airfoil Extruded to 3D

The first test case considered is for inviscid supersonic flow over a diamond airfoil, with chord length of one, and a thickness of 0.07 extruded to unit span in 3D. The free-stream Mach number is 2.0 and the angle of attack is 0 degrees. The test case has been used previously to verify various error estimates and adaptation mechanics for anisotropic meshes [11]. The dominant flow features include the wedge-shaped shocks at the leading and trailing edges, and the expansion fan emanating at the midchord. For the present study, a coarse mesh of 753 vertices is used as the initial mesh. This initial mesh and the poorly resolved Mach number are shown on Fig. 2. Mesh adaptations are performed based on the inviscid goal-oriented metric discussed in Section II.B. Drag coefficient is used as the output functional. Adaptations are done so that the target complexities, which decide the total number of degrees of freedom, are doubled after every five adaptation cycles.

An adapted grid (30th adaptation), having around 350,000 vertices and the well-resolved Mach number are shown in Fig. 3. The critical regions that contribute to the output functional are refined. The mesh convergence of drag coefficient is shown in Fig. 4. For comparison, the drag values obtained by mesh adaptation using the Mach interpolation error multiscale metric are also shown. The values plotted correspond to the last mesh at each fixed complexity. As expected, drag values based on the goal-oriented metric converges faster toward the fine-grid values compared to that of the multiscale metric. Figure 5 shows adapted grids based on both the multiscale metric and the goal-oriented metric, for roughly the same number of vertices. The multiscale adapted mesh, in order to reduce the interpolation error in Mach number, refines the shock all the way to the domain boundary, whereas the goal-oriented grid refines only those shock regions that contribute to the drag functional. The adjoint values are very small (see Fig. 6 a) away from the airfoil, indicating that residual errors in this region have little effect on the output functional. By not refining this region, the goal-oriented method places extra resolution near the airfoil, thereby making the drag coefficient more accurate.

Examination of the nearfield adjoint solution close in the vicinity of the shock reveals highly oscillatory solutions in this region, as seen in (Fig. 6 b). However, the boundary conditions on the symmetry planes, at $y = 0$ and $y = 1$, have been strongly enforced during the flow solution by explicitly initializing the normal velocity to zero, and subsequently modifying the corresponding rows in the matrix, as well as setting the associated residual to zero, to force zero updates during the solution process. When using strongly-enforced boundary conditions, as described above, the adjoint variables are arbitrary, and can exhibit highly oscillitory solutions [25]. By replacing the strongly-enforced boundary conditions on the symmetry planes with weakly enforced boundary conditions, the oscillations can be eliminated. The adjoint solution, corresponding to the x-momentum equations, is plotted along a slice spanning the upper shock at $z = 0.1$ in Fig. 7. Fig. 7(a) and Fig. 7(b) have been obtained using strongly-enforced symmetry boundary condition, whereas Fig. 7(c) and Fig. 7(d) correspond to solutions obtained using weakly-enforced boundary conditions. Values of

the velocity in the x-direction are also shown in both the plots to clearly delineate the shock location. In both cases, the shock is sharply resolved. However, as discussed above, the adjoint solution exhibits strong oscillations when the boundary conditions have been strongly implemented, whereas the adjoint solution is seen to be smooth across the shock when the weakly enforced boundary conditions are used. Interestingly, the drag convergence does not suffer when the strong boundary enforcement is used during the adaptation.

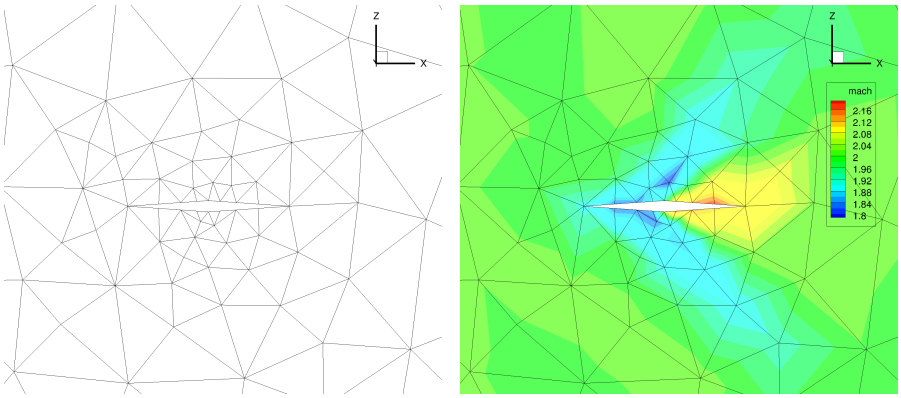


(a) Initial grid around the diamond airfoil. (b) Mach number.

**Fig. 2 Inviscid supersonic flow over extruded diamond airfoil, initial grid of 753 vertices.**

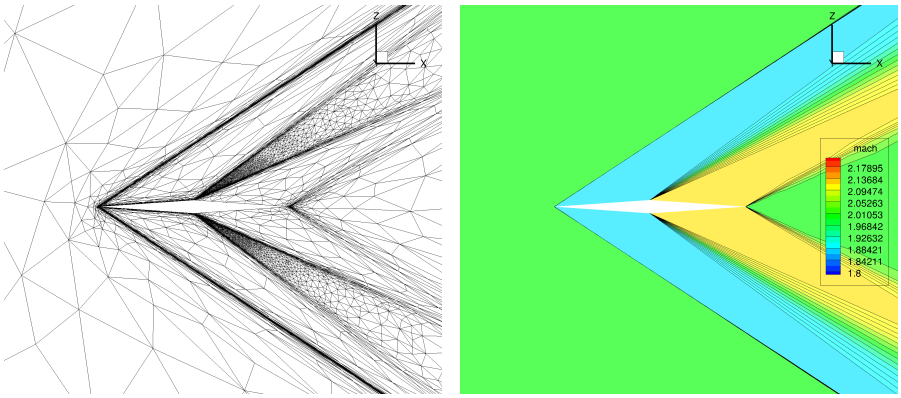


(a) Adapted grid. (b) Mach number.

**Fig. 3 Inviscid supersonic flow over extruded diamond airfoil, $30^{th}$ adapted grid (352,579 vertices) with drag output functional.**

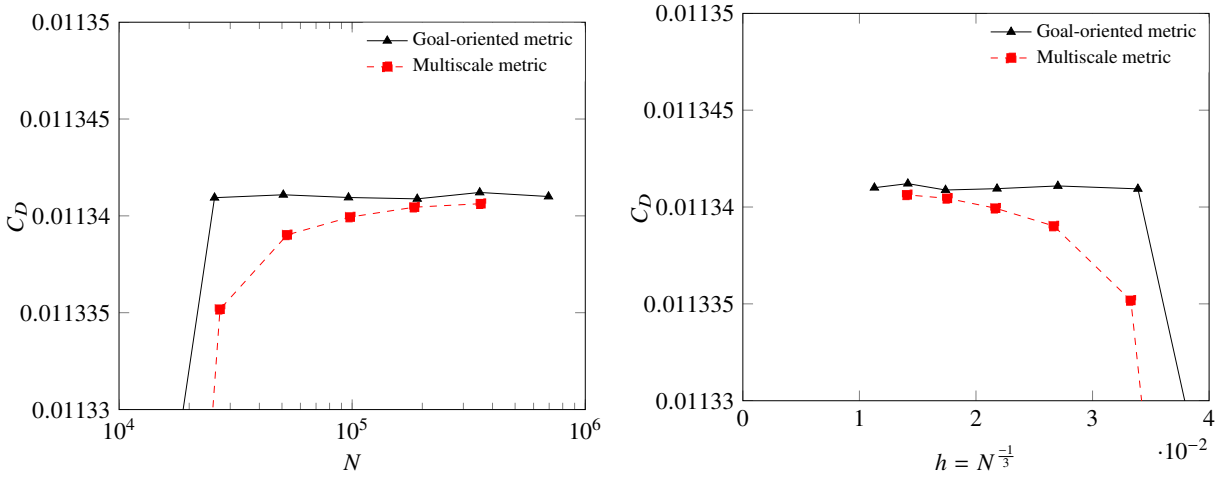


(a) Drag coefficient vs. Number of degrees of freedom (vertices).

(b) Drag coefficient vs. $h$.

**Fig. 4 Inviscid supersonic flow over extruded diamond airfoil, convergence of drag coefficient.**

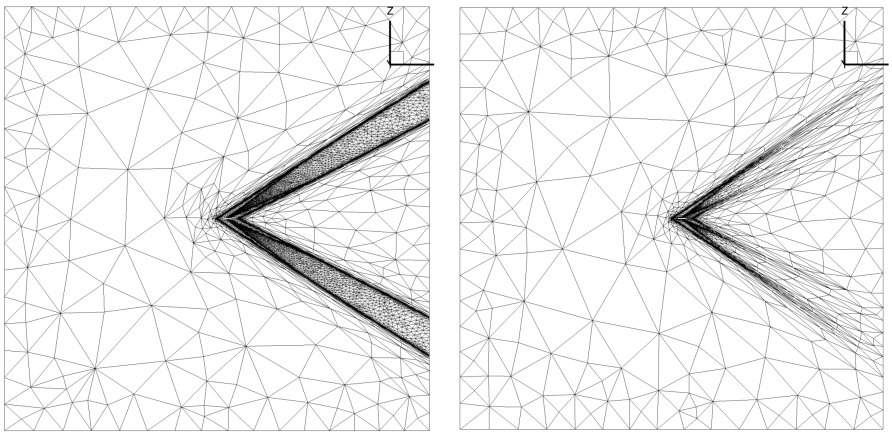


(a) Multiscale metric adapted grid.

(b) Goal-oriented metric adapted grid.

**Fig. 5 Inviscid supersonic flow over extruded diamond airfoil, comparison of multiscale and goal-oriented adapted grids at 190,000 vertices.**

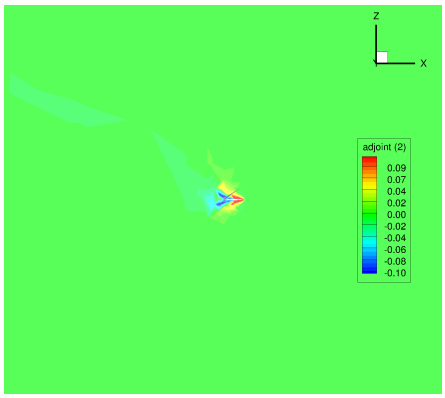


(a) x-momentum adjoint on goal-oriented metric adapted grid.

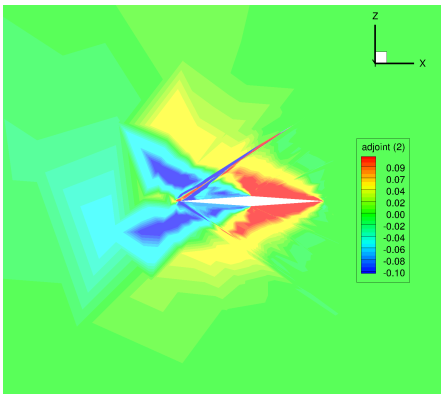


(b) x-momentum adjoint on goal-oriented metric adapted grid, zoomed view near airfoil.

**Fig. 6 Inviscid supersonic flow over extruded diamond airfoil, $x$-momentum adjoint contours.**

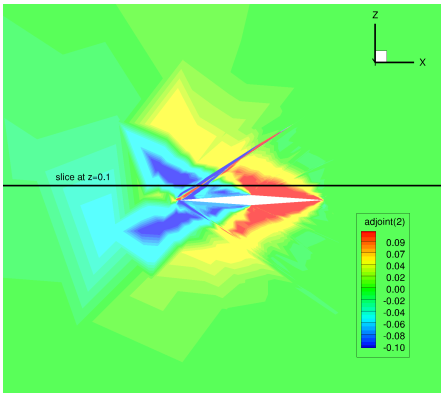


(a) x-momentum adjoint on grid at $y = 0$ plane with strongly enforced symmetry boundary condition.

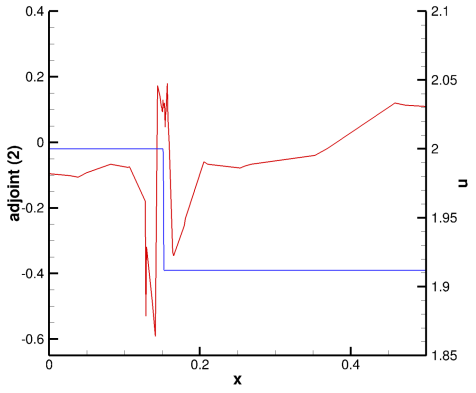


(b) x-momentum adjoint (red) and x-velocity (blue) near shock on a slice at $z = 0.1$.

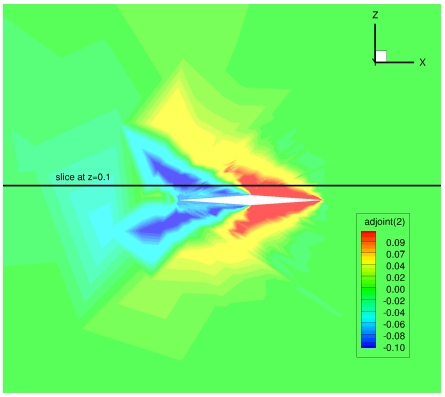


(c) x-momentum adjoint on grid at $y = 0$ plane with weakly enforced symmetry boundary condition.

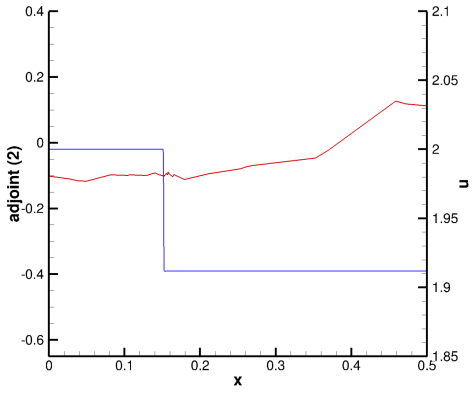


(d) x-momentum adjoint (red) and x-velocity (blue) near shock on a slice at $z = 0.1$.

**Fig. 7 Inviscid supersonic flow over extruded diamond airfoil, slicing at $z = 0.1$ to view the adjoint across the shock on grids with strongly enforced (top) and weakly enforced (bottom) symmetry boundary conditions.**

## IV. Numerical Results - Inviscid Flow over ONERA M6 Wing

The second test case is an inviscid, transonic flow over the ONERA M6 wing, where the free-stream Mach number is 0.84 and the angle of attack is 3.06 degrees. The ONERA M6 wing experiment was originally described in an AGARD report by Schmitt and Charpin [26], and has been widely used for CFD validation studies. The experimental data set consists of surface pressure coefficients at various spanwise sections on the wing for various Mach numbers and angles of attack at a Reynolds number of about 12 million. For the present numerical study, only inviscid simulations are performed for this geometry for the Mach number of 0.84 and angle of attack of 3.06 degrees. This corresponds to a transonic flow case with double shocks merging to form a 'lambda' shock on the upper surface of the wing. The geometry is modified to have a sharp trailing edge and a well-defined wing tip shape by Mayeur et al. [27, 28].

The computational domain and the coarse initial mesh around the wing are shown in Fig. 8. The farfield boundary is in the shape of a hemisphere nominally located at 100 chord lengths from the surface of the wing. The initial mesh consists of 6495 tetrahedral elements. Adjoint-based anisotropic mesh adaptations are performed using the drag force as the output functional. Figure 9 shows the mesh and the pressure field on the wing and symmetry plane, and Fig. 10 shows adjoint solutions corresponding to continuity, x-momentum, z-momentum, and energy equations, on the symmetry plane of the $32^{th}$ adapted mesh. Convergence of the drag coefficient for inviscid goal-oriented metric, along with that for the multiscale metric, is shown in Fig. 11. Both solutions appear to be converging toward the same fine-grid values. As expected, drag values from goal-oriented metrics are converging faster to the fine-grid values. For this test case, an additional goal-oriented adaptation has been performed where the drag force, used as the output functional, is calculated from the far-field boundary residuals instead of surface integration. It can be shown that, for a discretly conservative scheme, drag force calculated on the wing and on the farfield are identical. It is interesting to observe that the same drag convergence is obtained using either the farfield and nearfield drag computation as the output functionals. Adjoint values are also the same between the conputations, except for the x-momentum and z-momentum adjoints that are shifted by constant values [29]; the x-momentum adjoint is shifted by the cosine of the angle-of-attack whereas the z-momentum adjoint is shifted by the sine of the angle-of-attack (see Fig. 15).

Meshes, with nearly identical numbers of vertices, obtained using multiscale adaptation and goal-oriented adaptation are shown in Fig. 12. Multiscale metric, with the goal of minimizing the interpolation error, refines mostly at the shocks. Compared to the multiscale metric, the goal-oriented metric places less resolution at shocks, but more at the leading and trailing edges. The wing surface, in general, gets more resolution. Mesh resolution on the trailing edge near the root is compared for multiscale and goal-oriented metrics in Fig. 13 (a and b). The increased resolution from the goal-oriented metric is due to the high adjoint, and the adjoint derivatives, at the trailing edge as shown in Fig. 13 (c and d). Similar to trailing edge, the leading edge is also more highly refined using the goal-oriented metric (see Fig. 14), due to the high values of adjoint and its derivatives as evident from Fig. 14 (c and d).

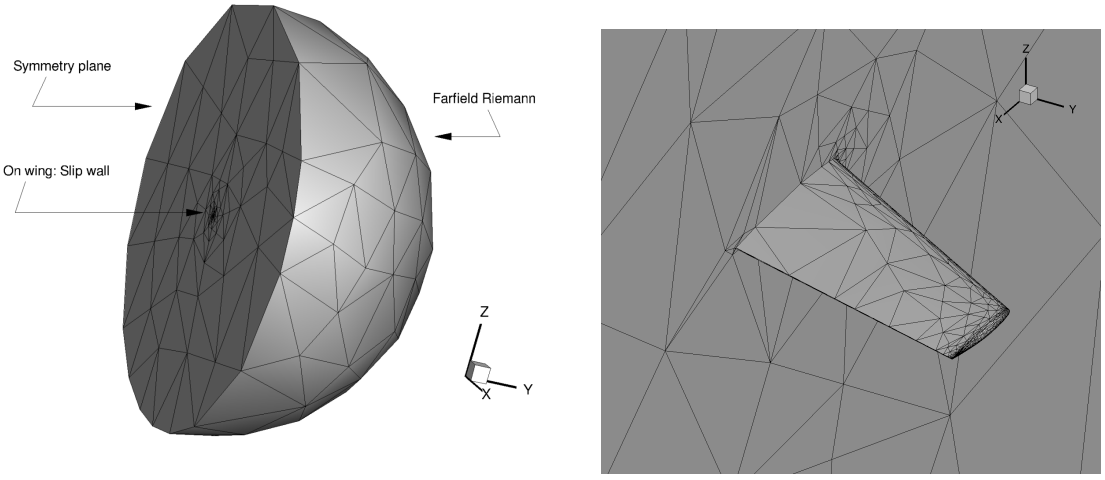


(a) Computational domain. (b) Wing and symmetry plane.

**Fig. 8 ONERA M6 initial grid.**

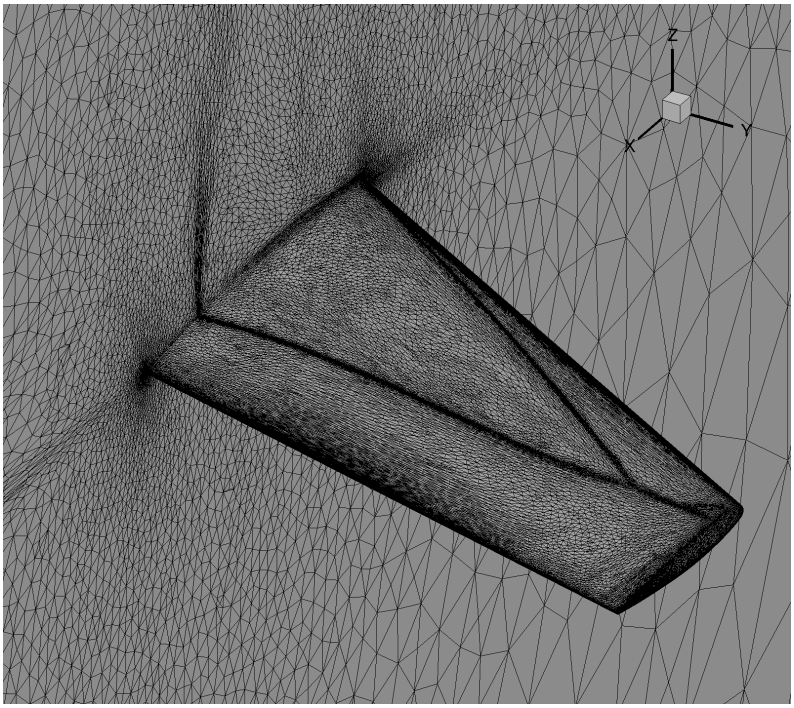


(a) Wing and symmetry plane.

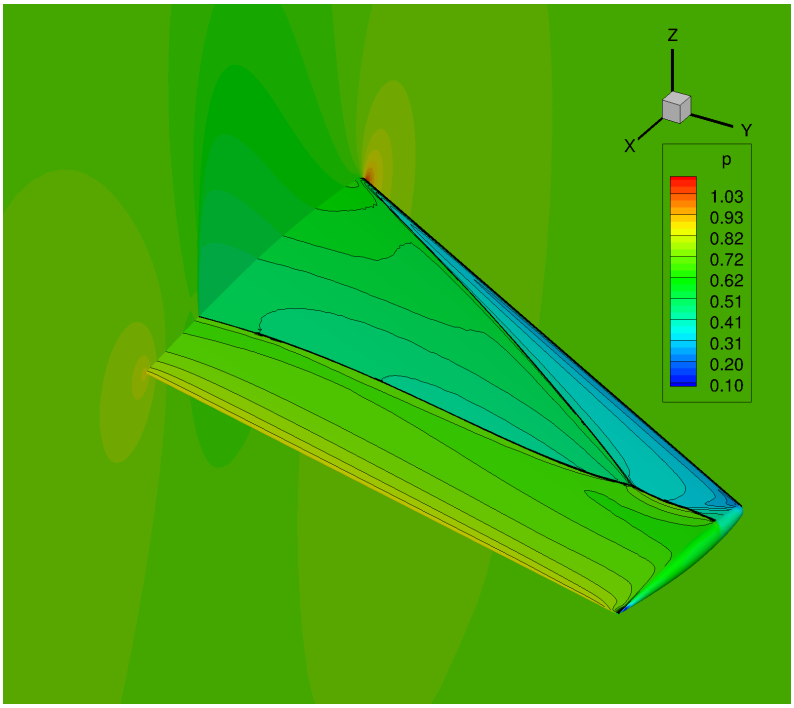


(b) Pressure contours.

**Fig. 9 Inviscid transonic flow over ONERA M6, $32^{th}$ adapted grid with drag output functional.**

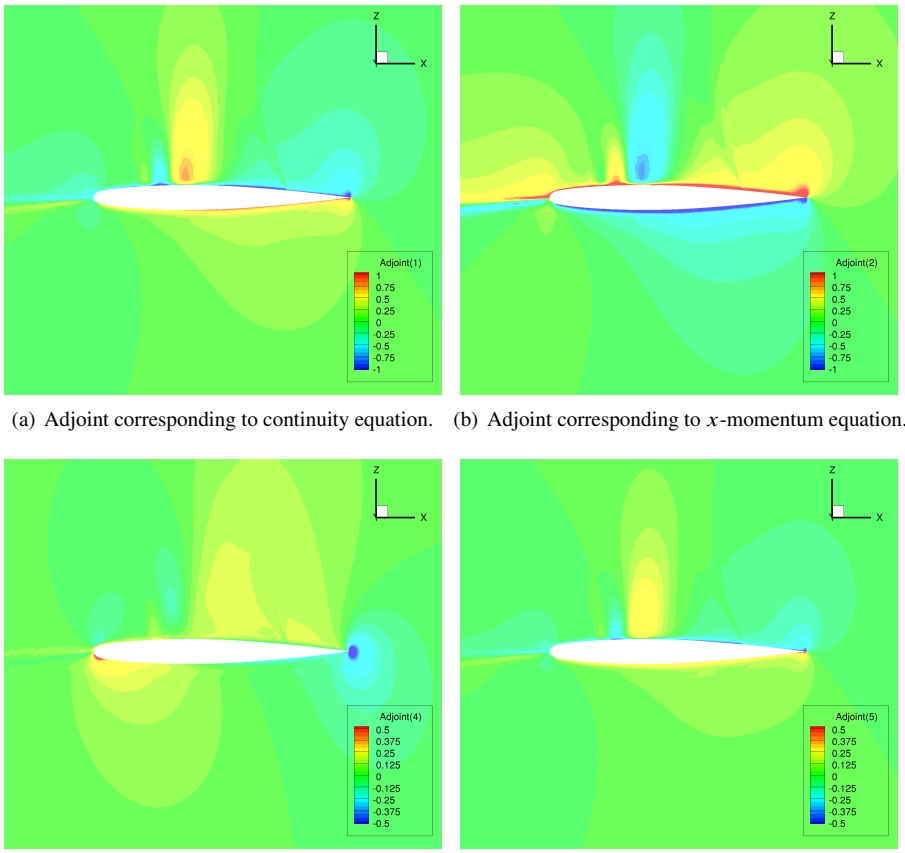


(a) Adjoint corresponding to continuity equation. (b) Adjoint corresponding to $x$-momentum equation.

(c) Adjoint corresponding to $z$-momentum equation. (d) Adjoint corresponding to energy equation.

**Fig. 10 Inviscid transonic flow over ONERA M6, contours of adjoint solutions on the symmetry plane.**

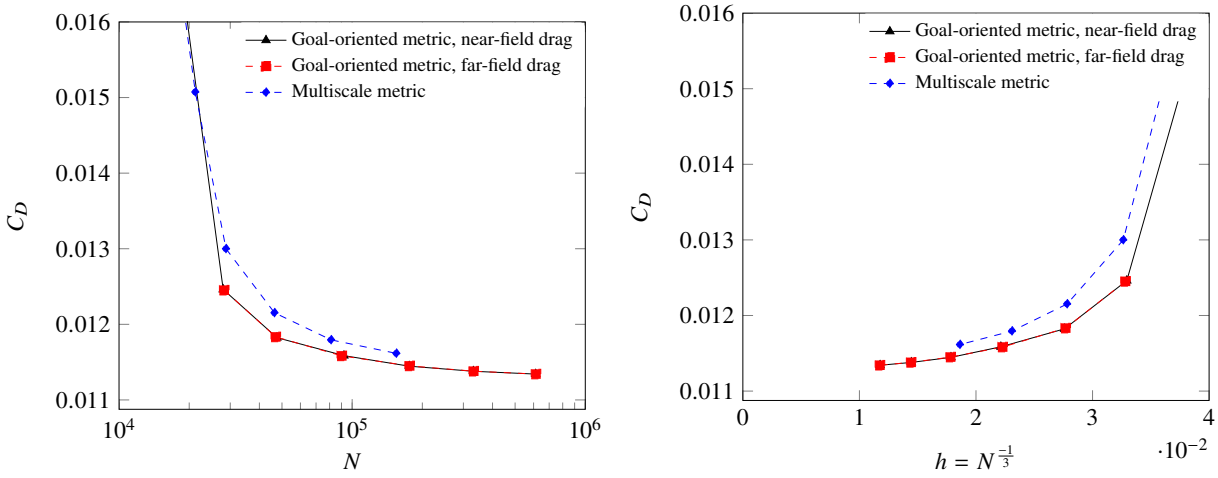


(a) Drag coefficient vs. Number of degrees of freedom (vertices). (b) Drag coefficient vs. $h$.

**Fig. 11 Inviscid transonic flow over ONERA M6 wing, convergence of drag coefficient.**

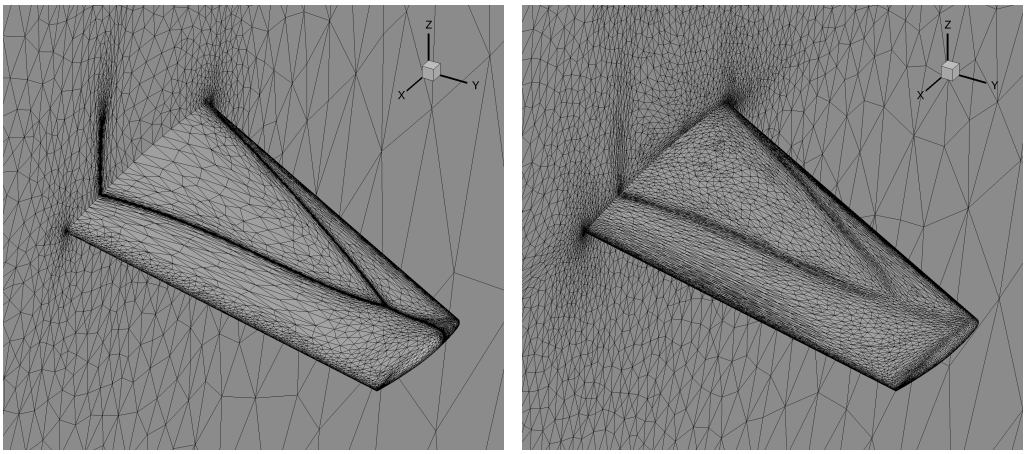

(a) Multiscale metric adapted mesh. (b) Goal-oriented metric adapted mesh.

**Fig. 12 Inviscid transonic flow over ONERA M6, comparison of multiscale and goal-oriented adaptations.**

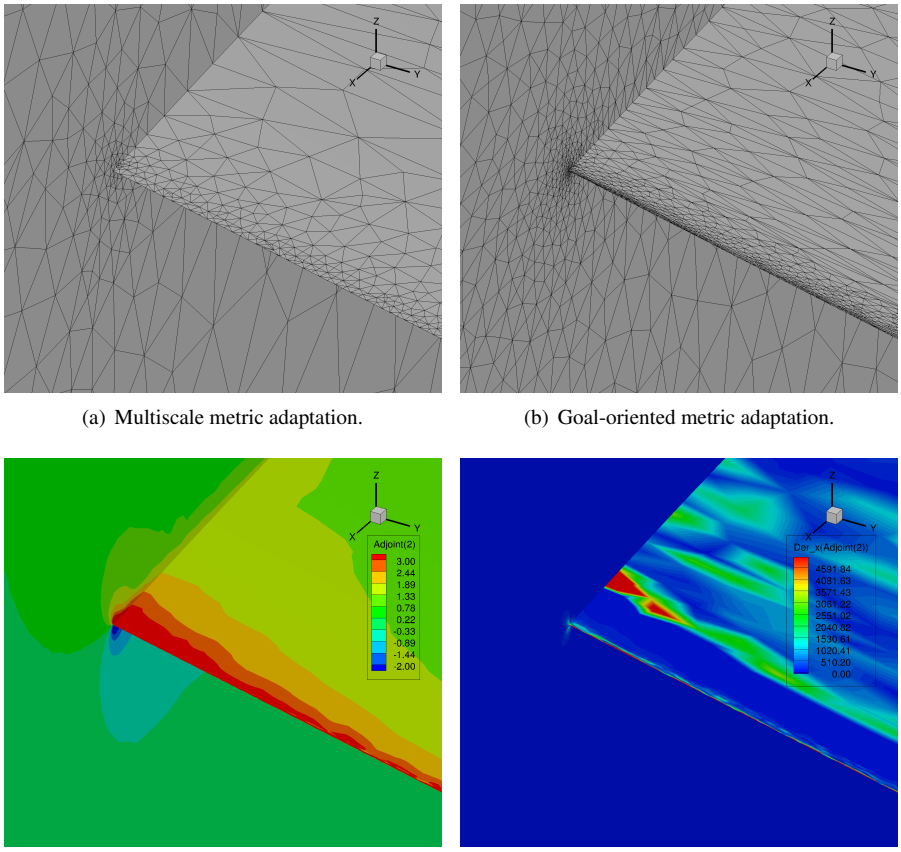


(a) Multiscale metric adaptation. (b) Goal-oriented metric adaptation.

(c) $x$-momentum adjoint on goal-oriented adapted mesh. (d) Absolute value of derivative of $x$-momentum adjoint in $x$-direction on goal-oriented adapted mesh.

**Fig. 13 Inviscid transonic flow over ONERA M6, view of wing trailing edge near symmetry plane, comparison of multiscale and goal-oriented adaptations.**

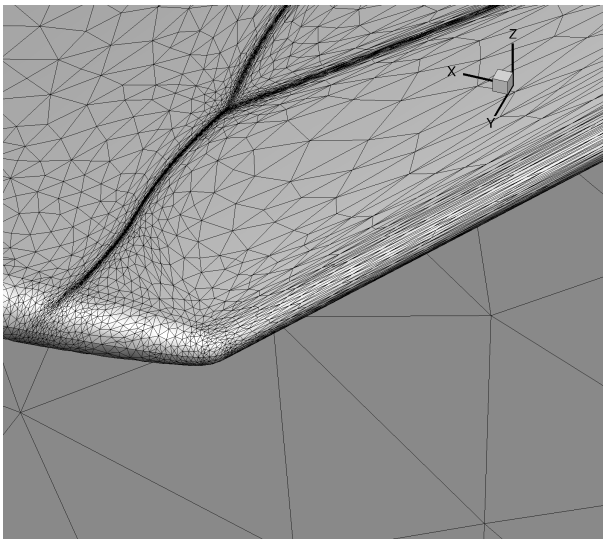


(a) Multiscale metric adaptation.

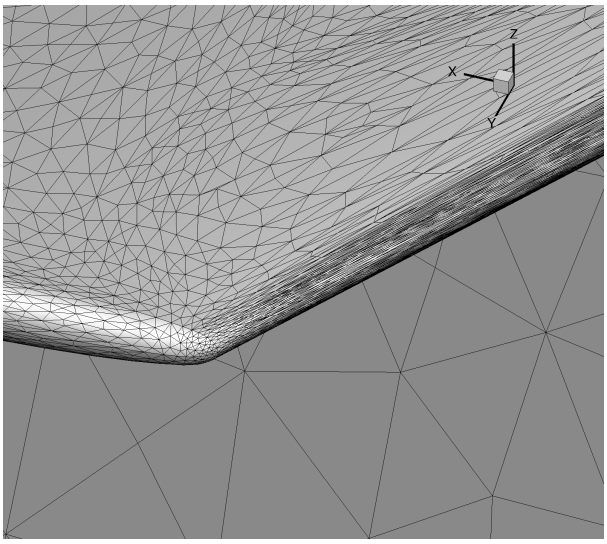


(b) Goal-oriented metric adaptation.

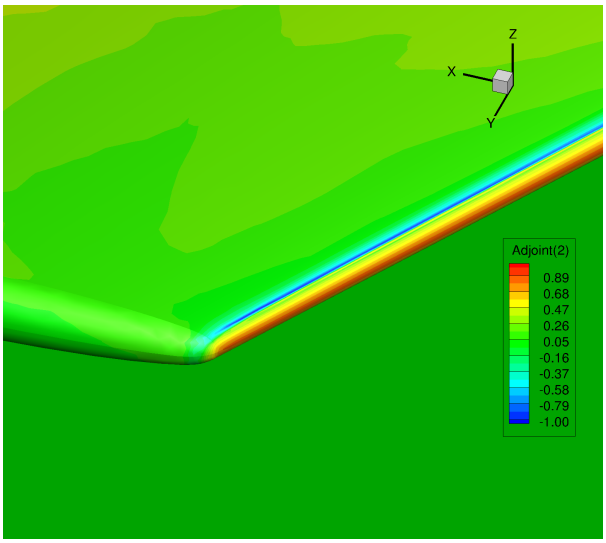


(c) $x$-momentum adjoint on the goal-oriented adapted grid

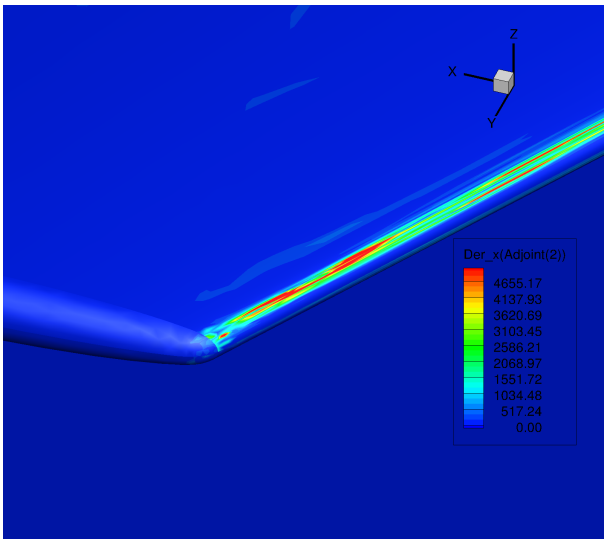


(d) Absolute value of derivative of $x$-momentum adjoint in $x$-direction on the goal-oriented adapted grid.

**Fig. 14 Inviscid transonic flow over ONERA M6, view of leading edge near the tip. comparison of multiscale and goal-oriented adaptations.**

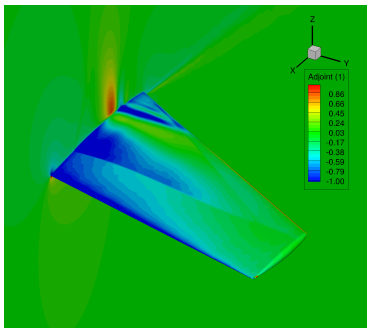

(a) continuity equation adjoint, drag computed on wing as output functional

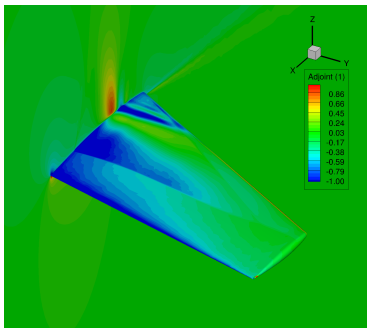

(b) continuity equation adjoint, drag computed on farfield as output functional

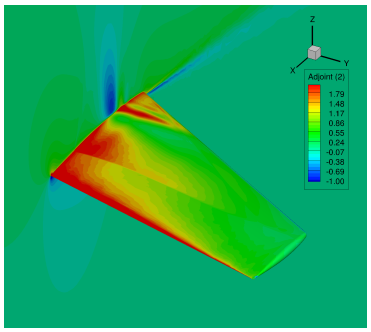

(c) x-momentum adjoint, drag computed on wing as output functional

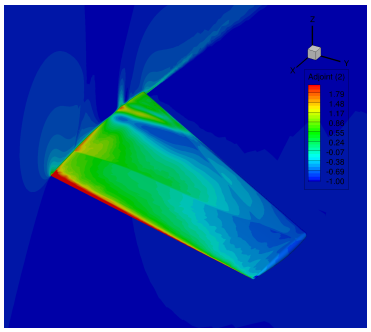

(d) x-momentum adjoint,drag computed on farfield as output functional

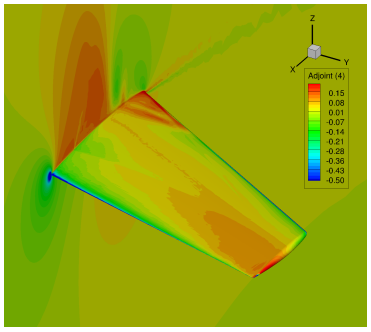

(e) z-momentum adjoint, drag computed on wing as output functional

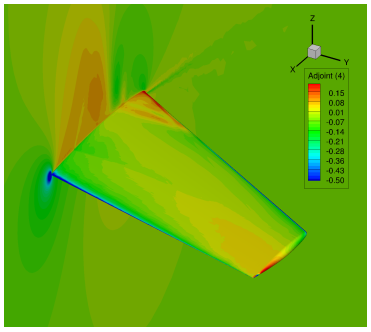

(f) z-momentum adjoint,drag computed on farfield as output functional

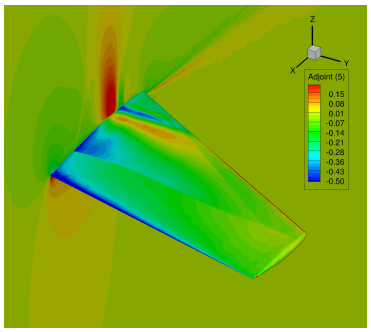

(g) energy equation adjoint, drag computed on wing as output functional

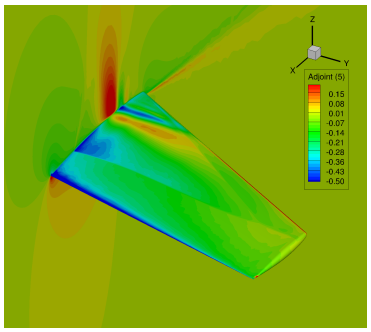

(h) energy equation adjoint,drag computed on farfield as output functional

**Fig. 15 Inviscid transonic flow ONERA M6 wing, comparison of adjoint values for drag on wing (left) and drag on farfield (right) as output functionals on the same grid.**

## V. Numerical Results - Laminar Subsonic Flow over Extruded NACA0012 Airfoil

The final test case is a laminar subsonic flow over an NACA0012 airfoil extruded to unit span in 3D. The free-stream Mach number is 0.5, the angle of attack is 3 degrees, and the Reynolds number is 5000 based on the chord of the airfoil. This test case, with various angle-of-attacks, has often been used to evaluate the accuracy and convergence of numerical algorithms, including high-order discretizations, for the Navier-stokes equations [30]. The critical flow feature is the flow separation starting at approximately 50% of the chord length on the suction side of the airfoil. This results in a primary and a secondary recirculation regions (see Fig. 19), which have to be resolved adequately. Venditti and Darmofal [31] have used this test case to demonstrate the efficiency of their output-based adaptation when compared to Hessian-based adaptation without the local scaling of the multiscale metric. Swanson and Langer [32] have recently performed a detailed analysis and grid-convergence study on both structured and unstructured grids for this test case. The study highlights the need to have proper mesh resolution in the neighborhood of the separation point and in the vicinity of the closure of the recirculation region in the wake, to obtain a steady state solution. Belme et al. [33] have developed an error estimate and the associated metric field for low Reynolds number Navier-Stokes equations, and used this test case to compare the drag convergence with those from interpolation error-based multiscale and inviscid goal-oriented metrics.

In the present work, the adaptation was initialized on a coarse mesh (1,857 vertices) with no boundary layer elements. The mesh and the Mach number contours are shown on Fig. 16. Target complexities are doubled after every five adaptation cycles. Figure 19 shows goal-oriented grid (21st adaptation) at the symmetry plane around the airfoil, Mach number contours along with the streamlines showing primary and secondary recirculation regions, and the adjoint corresponding to the momentum equations in the $x$-direction. All the critical regions including leading edge, boundary layer, recirculation zones are well resolved. Adjoint values are seen to be sufficiently smooth and high at the recirculation regions indicating residual perturbations in the region will have large influences on the drag coefficient. Convergence of drag coefficient, the output functional, is shown in Fig. 18. Convergence is also shown for adaptations based on inviscid goal-oriented metric, and the interpolation error-based multiscale metric. The drag coefficient from all three adaptations appear to be converging to a fixed value. The convergence based on both inviscid and viscous goal-oriented metric are seen to be similar, both of which are converging faster than the ones based on the multiscale metric adaptations. Figure 19 compares the grid produced by the multiscale metric (top) and the viscous opt-goal metric (bottom), for a similar number of degrees of freedom. Although both of them seem to have similar resolution in the wake region in the far view, a closer look (right figures) of the wake reveals that the multiscale metric puts a lot more resolution on the wake compared to the goal-oriented metric. Because the adjoint values are small far downstream of the wake, the goal-oriented metric does not put high resolution there compared to that of the multiscale metric.

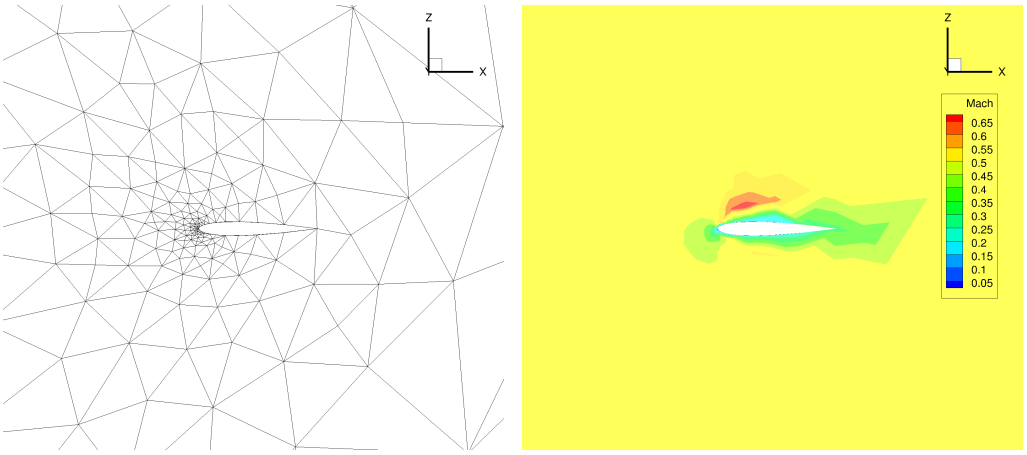


(a) Initial grid around the airfoil.

(b) Mach number contours.

**Fig. 16 Laminar subsonic flow around NACA0012, initial grid with 1,857 vertices.**

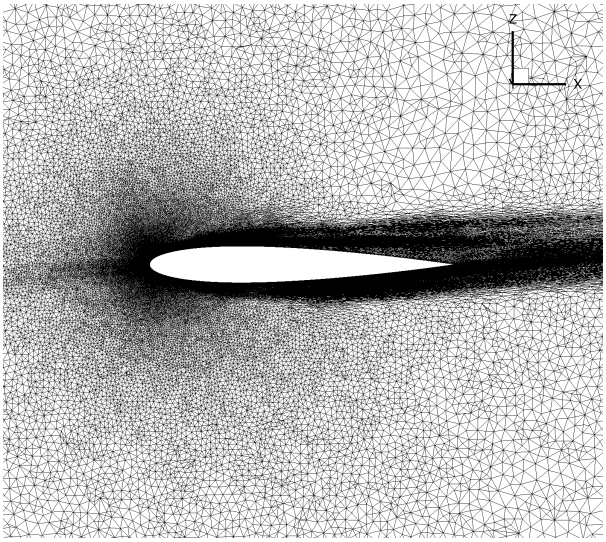


(a) 21st goal-oriented adapted grid.

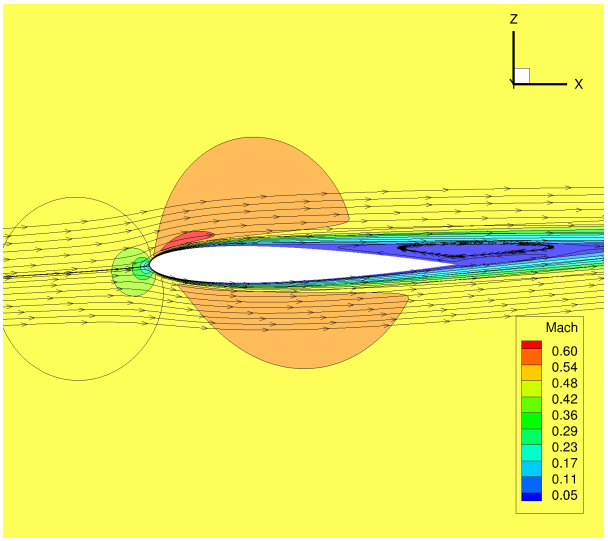


(b) Mach number contours and streamlines showing recirculation near the trailing edge.

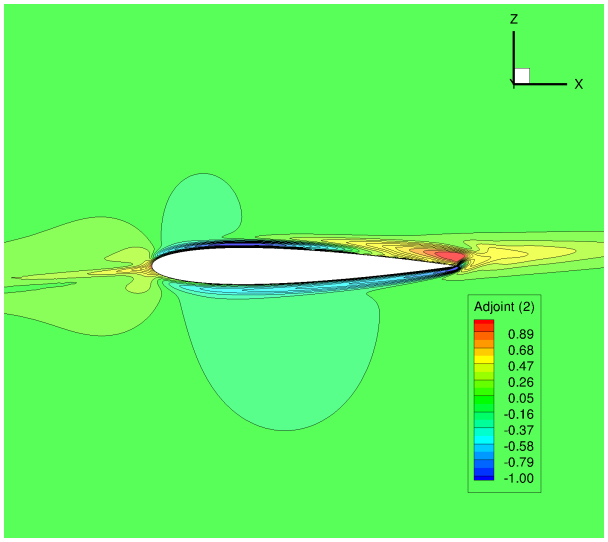


(c) Contours of $x$-momentum adjoint.

**Fig. 17 Laminar subsonic flow around NACA0012, 21st goal-oriented adapted grid with 280,000 vertices.**

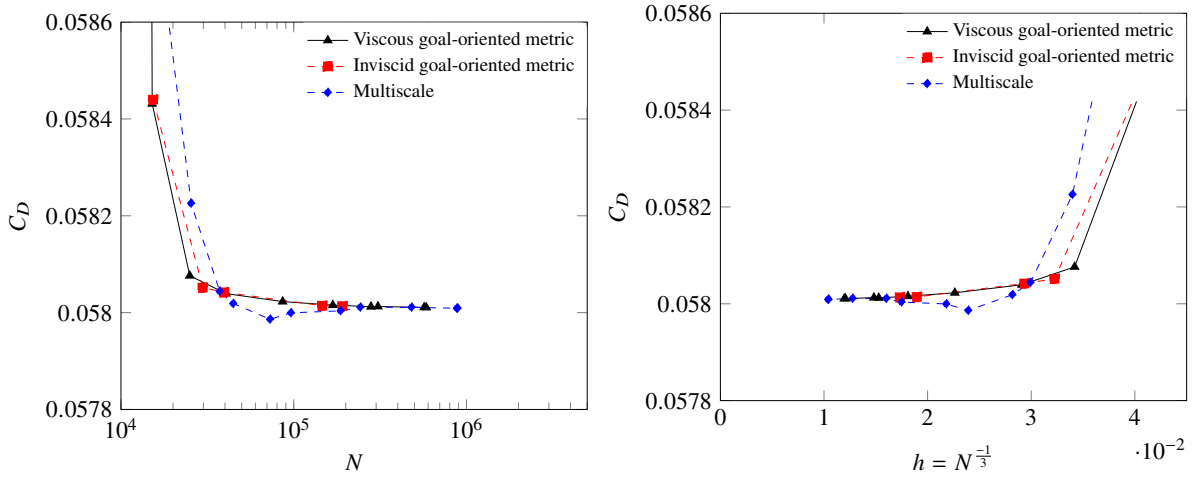


(a) Total drag coefficient vs. Number of degrees of freedom (vertices).

(b) Total drag coefficient vs. $h$.

**Fig. 18 Laminar subsonic flow around NACA0012, convergence of drag coefficient.**

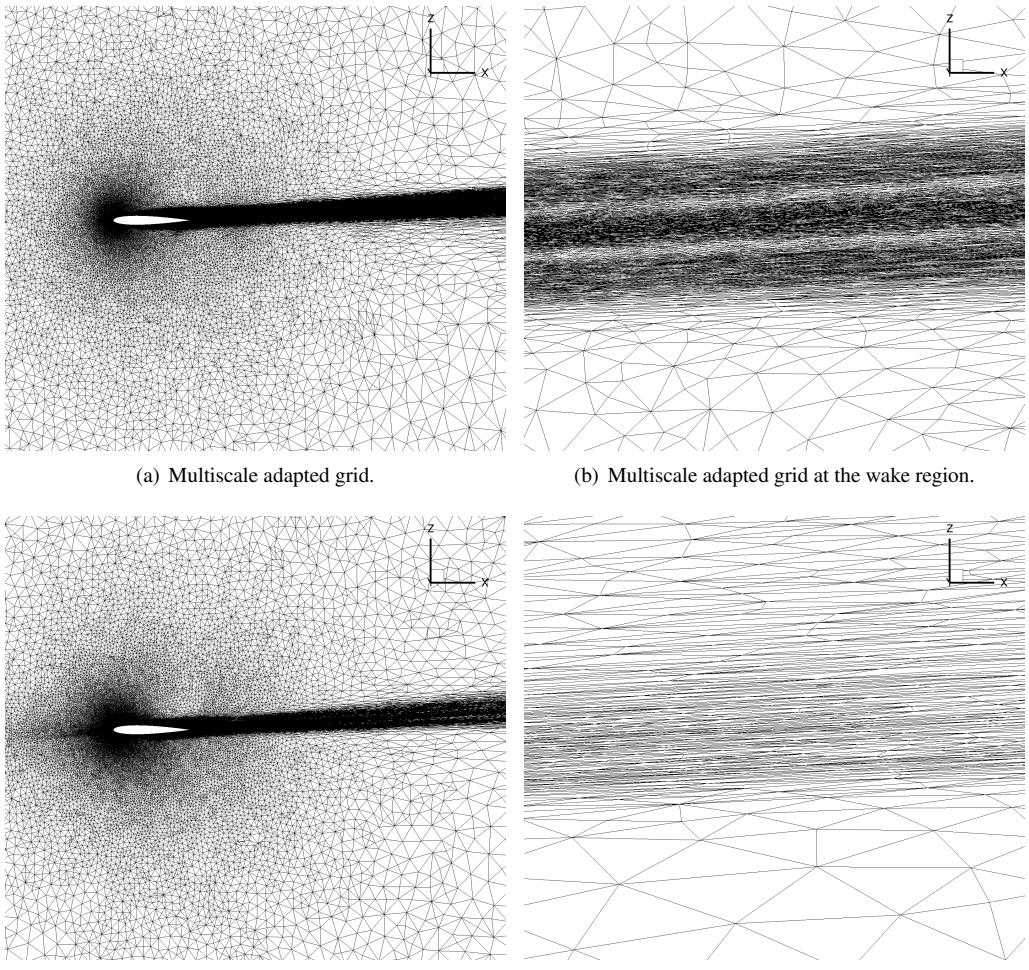


(a) Multiscale adapted grid.

(b) Multiscale adapted grid at the wake region.

(c) Goal-oriented adapted grid.

(d) Goal-oriented adapted grid at the wake region.

**Fig. 19 Laminar subsonic flow around NACA0012, comparison of multiscale and goal-oriented adapted grids.**

## VI. Conclusions

An adjoint solver has been implemented in the stabilized finite-element branch of the FUN3D flow solver, FUN3D-SFE, developed at the NASA Langley Research Center. The implementation of the adjoint has been verified by comparing the adjoint values with those obtained using a finite-difference method. Mesh adaptations have been performed, using drag coefficient as the output functional, for an inviscid supersonic flow around a diamond airfoil, and for a subsonic laminar flow around an NACA0012 airfoil, both extruded to 3D, and for an inviscid transonic flow around an ONERA M6 wing. For the inviscid cases, adaptations using a goal-oriented approach [7] were compared with results obtained using the multiscale metric that minimizes interpolation error in $L_p$ norm [14]. For the diamond airfoil case, it is demonstrated that using a strongly enforced symmetry boundary condition results in the adjoint solutions being highly oscillatory across the shock, where the mesh is most densly clustered. The oscillations are almost completely eliminated when the weakly-enforced boundary condition was used intead of the strongly-enforced ones. The drag convergence, however, is not noticeably adversly affected whether strong or weak enforcement is used. For the viscous case, adaptations have also been performed with a modified error estimate that augments the inviscid goal-oriented metric with viscous fluxes. For the presented case, the convergence of the drag coefficient has been found to be similar for both goal-oriented methods. Drag convergence using both inviscid goal-oriented metric and the viscous goal-oriented metric have been observed to be faster compared to that of the multiscale approach. Future work will focus on developing adjoint-based error estimates, and robust adaptation strategy for turbulent flows governed by RANS equations.

## Acknowledgments

This research was sponsored by the NASA Transformational Tools and Technologies (TTT) Project of the Transformative Aeronautics Concepts Program under the Aeronautics Research Mission Directorate.

## References

[1] Slotnick, J., Khodadoust, A., Alonso, J., Darmofal, D., Gropp, W., Lurie, E., and Mavriplis, D., "CFD Vision 2030 Study: A Path to Revolutionary Computational Aerosciences," NASA CR-2014-218178, Langley Research Center, Mar. 2014. doi:2060/20140003093.

[2] Anderson, W. K., Newman, J. C., and Karman, S. L., "Stabilized Finite Elements in FUN3D," *Journal of Aircraft*, Vol. 55, No. 2, 2018, pp. 696–714. doi:10.2514/1.C034482.

[3] Biedron, R. T., Carlson, J.-R., Derlaga, J. M., Gnoffo, P. A., Hammond, D. P., Jones, W. T., Kleb, B., Lee-Rausch, E. M., Nielsen, E. J., Park, M. A., Rumsey, C. L., Thomas, J. L., and Wood, W. A., "FUN3D Manual: 13.4," NASA TM-2018-220096, Langley Research Center, Oct. 2018. doi:2060/20180007519.

[4] Leicht, T., and Hartmann, R., "Error Estimation and Anisotropic Mesh Refinement for 3D Laminar Aerodynamic Flow Simulations," *Journal of Computational Physics*, Vol. 229, No. 19, 2010, pp. 7344–7366. doi:10.1016/j.jcp.2010.06.019.

[5] Loseille, A., and Alauzet, F., "Continuous Mesh Framework Part I: Well-Posed Continuous Interpolation Error," *SIAM Journal on Numerical Analysis*, Vol. 49, No. 1, 2011, pp. 38–60. doi:10.1137/090754078.

[6] Loseille, A., and Alauzet, F., "Continuous Mesh Framework Part II: Validations and Applications," *SIAM Journal on Numerical Analysis*, Vol. 49, No. 1, 2011, pp. 61–86. doi:10.1137/10078654X.

[7] Loseille, A., Dervieux, A., and Alauzet, F., "Fully Anisotropic Goal-Oriented Mesh Adaptation for 3D Steady Euler Equations," *Journal of Computational Physics*, Vol. 229, No. 8, 2010, pp. 2866–2897. doi:10.1016/j.jcp.2009.12.021.

[8] Fidkowski, K. J., and Darmofal, D. L., "Review of Output-Based Error Estimation and Mesh Adaptation in Computational Fluid Dynamics," *AIAA Journal*, Vol. 49, No. 4, 2011, pp. 673–694. doi:10.2514/1.J050073.

[9] Alauzet, F., and Loseille, A., "A Decade of Progress on Anisotropic Mesh Adaptation for Computational Fluid Dynamics," *Computer-Aided Design*, Vol. 72, 2016, pp. 13–39. doi:10.1016/j.cad.2015.09.005, 23rd International Meshing Roundtable Special Issue: Advances in Mesh Generation.

[10] Park, M. A., Krakos, J. A., Michal, T., Loseille, A., and Alonso, J. J., "Unstructured Grid Adaptation: Status, Potential Impacts, and Recommended Investments Toward CFD Vision 2030," AIAA Paper 2016–3323, 2016.

[11] Park, M. A., Loseille, A., Krakos, J. A., and Michal, T., "Comparing Anisotropic Output-Based Grid Adaptation Methods by Decomposition," AIAA Paper 2015–2292, 2015.

[12] Park, M. A., Barral, N., Ibanez, D., Kamenetskiy, D. S., Krakos, J., Michal, T., and Loseille, A., "Unstructured Grid Adaptation and Solver Technology for Turbulent Flows," AIAA Paper 2018–1103, 2018.

[13] Park, M. A., Balan, A., Anderson, W. K., Galbraith, M. C., Caplan, P. C., Carson, H. A., Michal, T., Krakos, J. A., Kamenetskiy, D. S., Loseille, A., Alauzet, F., Frazza, L., and Barral, N., "Verification of Unstructured Grid Adaptation Components," AIAA Paper 2019–1723, 2019.

[14] Loseille, A., Dervieux, A., Frey, P. J., and Alauzet, F., "Achievement of Global Second Order Mesh Convergence for Discontinuous Flows with Adapted Unstructured Meshes," AIAA Paper 2007–4186, 2007.

[15] Brooks, A. N., and Hughes, T. J. R., "Streamline Upwind/Petrov-Galerkin Formulation for Convection Dominated Flows with Particular Emphasis on Incompressible Navier-Stokes Equations," *Computer Methods in Applied Mechanics and Engineering*, Vol. 32, No. 1–3, 1982, pp. 199–259. doi:10.1016/0045-7825(82)90071-8.

[16] Shakib, F., Hughes, T. J. R., and Johan, Z., "A New Finite-Element Formulation for Computational Fluid Dynamics: X. The Compressible Euler and Navier-Stokes Equations," *Computer Methods in Applied Mechanics and Engineering*, Vol. 89, No. 1–3, 1991, pp. 141–219. doi:10.1016/0045-7825(91)90041-4.

[17] Hughes, T. J. R., Franca, L. P., and Hulbert, G. M., "A New Finite-Element Formulation for Computational Fluid Dynamics: VIII. The Galerkin Least Squares Method for Advective-Diffusion Equations," *Computer Methods in Applied Mechanics and Engineering*, Vol. 73, No. 2, 1989, pp. 173–189. doi:10.1016/0045-7825(89)90111-4.

[18] Bazilevs, Y., and Akkerman, I., "Large Eddy Simulation of Turbulent Taylor–Couette Flow Using Isogeometric Analysis and the Residual-Based Variational Multiscale Method," *Journal of Computational Physics*, Vol. 229, No. 9, 2010, pp. 3402–3414. doi:10.1016/j.jcp.2010.01.008.

[19] Allmaras, S. R., Johnson, F. T., and Spalart, P. R., "Modifications and Clarifications for the Implementation of the Spalart-Allmaras Turbulence Model," *Seventh International Conference on Computational Fluid Dynamics (ICCFD7)*, 2012.

[20] Loseille, A., Frazza, L., and Alauzet, F., "Comparing Anisotropic Adaptive Strategies on the 2nd AIAA Sonic Boom Workshop Geometry," *AIAA Journal of Aircraft*, 2018. doi:10.2514/1.C034840.

[21] Barth, T. J., "Recent Developments in High Order K-Exact Reconstruction on Unstructured Meshes," AIAA Paper 93–668, 1993.

[22] Michal, T., and Krakos, J., "Anisotropic Mesh Adaptation Through Edge Primitive Operations," AIAA Paper 2012–159, 2012.

[23] Alauzet, F., "A Changing-Topology Moving Mesh Technique for Large Displacements," *Engineering with Computers*, Vol. 30, No. 2, 2014, pp. 175–200. doi:10.1007/s00366-013-0340-z.

[24] Haimes, R., and Drela, M., "On The Construction of Aircraft Conceptual Geometry for High-Fidelity Analysis and Design," AIAA Paper 2012–683, 2012.

[25] Anderson, W. K., and Venkatakrishnan, V., "Aerodynamic Design Optimization on Unstructured Grids with a Continuous Adjoint Formulation," *Computers and Fluids*, Vol. 28, No. 4–5, 1999, pp. 443–480. doi:10.1016/S0045-7930(98)00041-3.

[26] Schmitt, V., and Charpin, F., "Pressure Distributions on the ONEAR-M6-Wing at Transonic Mach Numbers," *Experimental Data Base for Computer Program Assessment: Report of the Fluid Dynamics Panel Working Group 04*, AR-138, NATO Research and Technology Organisation AGARD, 1979, pp. B1:1–B1:44.

[27] Mayeur, J., Dumont, A., Destarac, D., and Gleize, V., "Reynolds-Averaged Navier–Stokes Simulations on NACA0012 and ONERA-M6 Wing with the ONERA elsA Solver," *AIAA Journal*, Vol. 54, No. 9, 2016, pp. 2671–2687. doi:10.2514/1.J054512.

[28] Mayeur, J., Dumont, A., Destarac, D., and Gleize, V., "RANS Simulations on TMR 3D Test Cases with the ONERA elsA Flow Solver," AIAA Paper 2016–1357, 2016.

[29] Fidkowski, K. J., Ceze, M. A., and Roe, P. L., "Entropy-Based Drag-Error Estimation and Mesh Adaptation in Two Dimensions," *AIAA Journal of Aircraft*, Vol. 49, No. 5, 2012, pp. 1485–1496.

[30] Wang, Z. J., Fidkowski, K., Abgrall, R., Bassi, F., Caraeni, D., Cary, A., Deconinck, H., Hartmann, R., Hillewaert, K., Huynh, H. T., Kroll, N., May, G., Persson, P.-O., van Leer, B., and Visbal, M., "High-Order CFD Methods: Current Status and Perspective," *International Journal for Numerical Methods in Fluids*, Vol. 72, No. 8, 2013, pp. 811–845. doi:10.1002/fld.3767.

[31] Venditti, D. A., and Darmofal, D. L., "Anisotropic Grid Adaptation for Functional Outputs: Application to Two-Dimensional Viscous Flows," *Journal of Computational Physics*, Vol. 187, No. 1, 2003, pp. 22–46. doi:10.1016/S0021-9991(03)00074-3.

[32] Swanson, R. C., and Langer, S., "Steady-State Laminar Flow Solutions for NACA 0012 Airfoil," *Journal of Computational Physics*, Vol. 126, 2016, pp. 102–128. doi:10.1016/j.compfluid.2015.11.009.

[33] Belme, A., Alauzet, F., and Dervieux, A., "An a priori Anisotropic Goal-Oriented Error Estimate for Viscous Compressible Flow and Application to Mesh Adaptation," *Journal of Computational Physics*, Vol. 376, 2019, pp. 1051–1088. doi:10.1016/j.jcp.2018.08.048.